ARL-TR-9020 • Aug 2020

DEVCOM
ARMY RESEARCH
LABORATORY

Higher Time-Resolution LASEM, Part I: Influence of Aluminum Morphology on Laser-Induced Shock Waves and Chemistry

by Jennifer L Gottfried

NOTICES

Disclaimers

ARL-TR-9020 ● AUG 2020

Higher Time-Resolution LASEM, Part I: Influence of Aluminum Morphology on Laser-Induced Shock Waves and Chemistry

Jennifer L Gottfried
Weapons and Materials Research Directorate, CCDC Army Research Laboratory

REPORT DOCUMENTATION PAGE	*Form Approved* *OMB No. 0704-0188*

1. REPORT DATE *(DD-MM-YYYY)* August 2020	**2. REPORT TYPE** Technical Report	**3. DATES COVERED (From - To)** 21 November 2019–20 June 2020

4. TITLE AND SUBTITLE Higher Time-Resolution LASEM, Part I: Influence of Aluminum Morphology on Laser-Induced Shock Waves and Chemistry	**5a. CONTRACT NUMBER**
	5b. GRANT NUMBER
	5c. PROGRAM ELEMENT NUMBER
6. AUTHOR(S) Jennifer L Gottfried	**5d. PROJECT NUMBER** 622141AH6RK16
	5e. TASK NUMBER
	5f. WORK UNIT NUMBER
7. PERFORMING ORGANIZATION NAME(S) AND ADDRESS(ES) CCDC Army Research Laboratory ATTN: FCDD-RLW-LB Aberdeen Proving Ground, MD 21005	**8. PERFORMING ORGANIZATION REPORT NUMBER** ARL-TR-9020
9. SPONSORING/MONITORING AGENCY NAME(S) AND ADDRESS(ES)	**10. SPONSOR/MONITOR'S ACRONYM(S)**
	11. SPONSOR/MONITOR'S REPORT NUMBER(S)

12. DISTRIBUTION/AVAILABILITY STATEMENT

Approved for public release; distribution is unlimited.

13. SUPPLEMENTARY NOTES

ORCID ID: Jennifer Gottfried, 0000-0002-1282-1928

14. ABSTRACT

Previous work demonstrated the differences in plasma plume and combustion dynamics following the pulsed-laser excitation of aluminum (Al) samples with different morphology. Here, a newly upgraded laser-induced air shock from energetic materials (LASEM) system with improved time-resolution and diagnostic capabilities was used to investigate the influence of Al morphology on the energy release rates (microsecond and millisecond timescales) and the high-temperature chemistry. Our results confirm that more Al nanoparticles react on the microsecond timescale than micron-sized Al particles, resulting in stronger laser-induced shock velocities and increased aluminum monoxide emission. This data provides insights into the mechanisms for Al oxidation that could lead to advancements in the development of aluminized formulations for enhanced energetic performance.

15. SUBJECT TERMS

aluminum, nanoparticles, laser-induced air shock from energetic materials, LASEM, laser-induced shock wave, emission spectroscopy

16. SECURITY CLASSIFICATION OF:			**17. LIMITATION OF ABSTRACT**	**18. NUMBER OF PAGES**	**19a. NAME OF RESPONSIBLE PERSON** Jennifer L Gottfried
a. REPORT Unclassified	**b. ABSTRACT** Unclassified	**c. THIS PAGE** Unclassified	UU	48	**19b. TELEPHONE NUMBER (Include area code)** (410) 278-7573

Standard Form 298 (Rev. 8/98)
Prescribed by ANSI Std. Z39.18

Contents

List of Figures

List of Tables

Acknowledgments

The author wishes to thank Dr Brian Barnes for developing an edge detection algorithm to measure the laser-induced shock wave positions and providing results used in this report. The author also thanks Dr Steven Dean for his assistance setting up the dual monochromator/photomultiplier tubes used to track the time-resolved emission of particular species. This project was primarily funded by the US Army Combat Capabilities Development Command (CCDC) Army Research Laboratory's (ARL's) 6.2 Energetics Mission Program in support of the CCDC Army Research Laboratory's Long-Range Distributed and Collaborative Engagements essential research area and the Army's top modernization priority Long-Range Precision Fires. Funding for new diagnostic equipment was provided by the US Department of Defense, Office of the Under Secretary for Defense for Research and Engineering, Applied Research for the Advancement of Science and Technology Priorities Program on Enhanced Energetic Effects under Task 2: Accelerating MAGIC (Materials Adding Gurney through Inorganic Chemistry).

1. Introduction

Nanosecond-pulsed laser ablation is commonly used for rapid, high-throughput characterization of material properties.[1,2] Significant effort has been expended to understand the influence of laser parameters such as fluence, wavelength, or pulse duration and environmental conditions such as atmospheric pressure or composition on the resulting material ablation and laser-induced plasma formation. However, the effects of sample morphology and chemical reactivity have rarely been investigated. Here, we use new laser-based diagnostic capabilities to explore these effects on aluminum (Al) samples.

Aluminum is of interest as an energetic material additive to enhance the performance of conventional military explosives and propellant formulations. Aluminum is a high-energy density material with a heat of combustion of 31 kJ/g; for comparison, the heats of detonation and combustion of the explosive TNT are 4.5 and 14.5 kJ/g, respectively. Aluminum particles react spontaneously in air to form an oxide shell (alumina [Al_2O_3]), which serves as a barrier to ignition (T_{ign} ~2350 K) and delays the oxidation of the Al core. Particles of Al tens of micrometers in diameter (micron-Al) are currently used in explosive formulations to enhance late time blast effects or increase bubble energy for underwater explosives, and to influence the burn rate or specific impulse of propellants. Aluminum nanoparticles (nano-Al) have a much larger specific surface area; since the surface atoms are more reactive, the ignition temperatures rapidly drop with decreasing particle size (down to ~1000 K for 100-nm particles).[3] Thus, more nano-Al is expected to react at earlier times during a detonation event and may be able to influence the Gurney energy (i.e., metal-pushing ability) and/or detonation velocity (i.e., metal-shattering ability). Another difference is that unlike larger micron-sized particles, the particle temperatures for nanoparticles are determined by the surrounding environmental temperatures. However, nano-Al provides its own set of challenges such as the high percentage of parasitic mass due to the Al_2O_3 shell, a strong tendency to agglomerate, the pyrophoric nature of unpassivated nano-Al, and difficulties with ageing and formulation properties. Commercial samples of both micron-Al and nano-Al are readily available. In addition, the laser ablation of bulk Al leads to the formation of Al particles, the size of which depends on the laser pulse energy and other experimental conditions.[4–7] Figure 1 summarizes some of the differences between micron-Al and nano-Al particle properties and behavior.

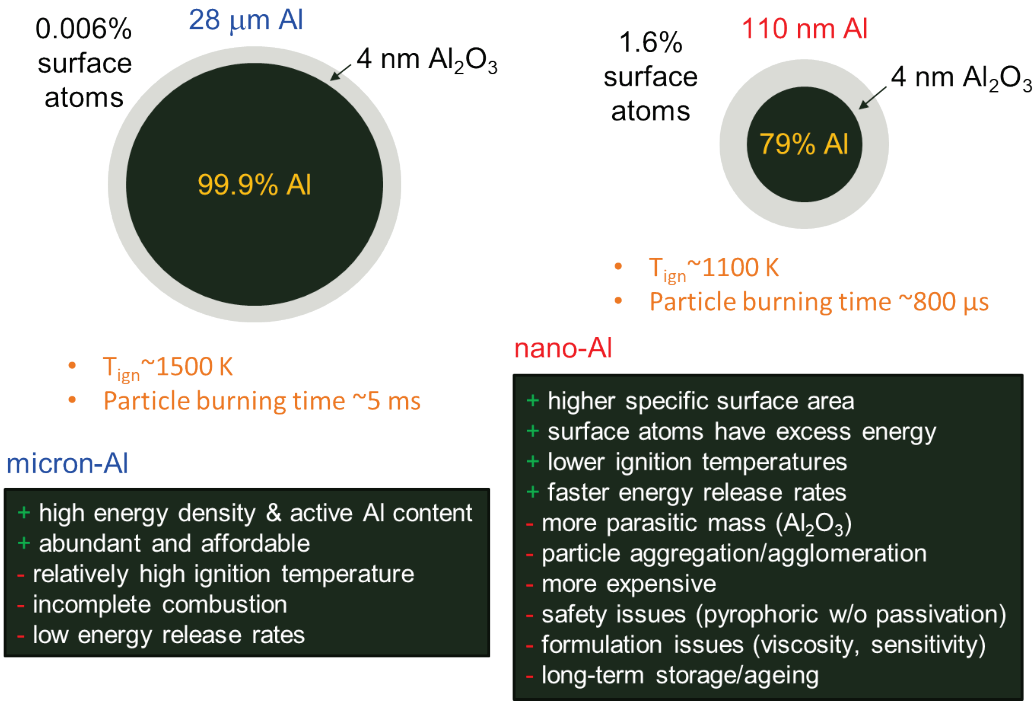

Fig. 1 **Aluminum particle size effects. Ignition temperatures and particle burning times estimated from Yetter et al.[3] The theoretical active Al content for each particle size (calculated based on an assumed oxide layer thickness of 4 nm) is shown in yellow.**

Recently, we used fast, gated emission spectroscopy and a high-speed framing camera to determine the intensity and spatiotemporal evolution of various Al ablation products following formation of a laser-induced plasma in air. The effect of Al morphology and oxidative reactivity were investigated using a high-purity Al plate, micron-Al, nano-Al, and micron-Al_2O_3 powders.[8] Distinct differences in the laser–material interaction for 1) bulk versus powder Al, 2) reactive versus nonreactive micron powders, and 3) micron-Al versus nano-Al were observed (Fig. 2). For example, the laser-induced plasma expansion and combustion dynamics of micron-Al and nano-Al powders were quite distinct (Fig. 2a) because of differences in the species distribution (Fig. 2b) and temperature regions (Fig. 2c).

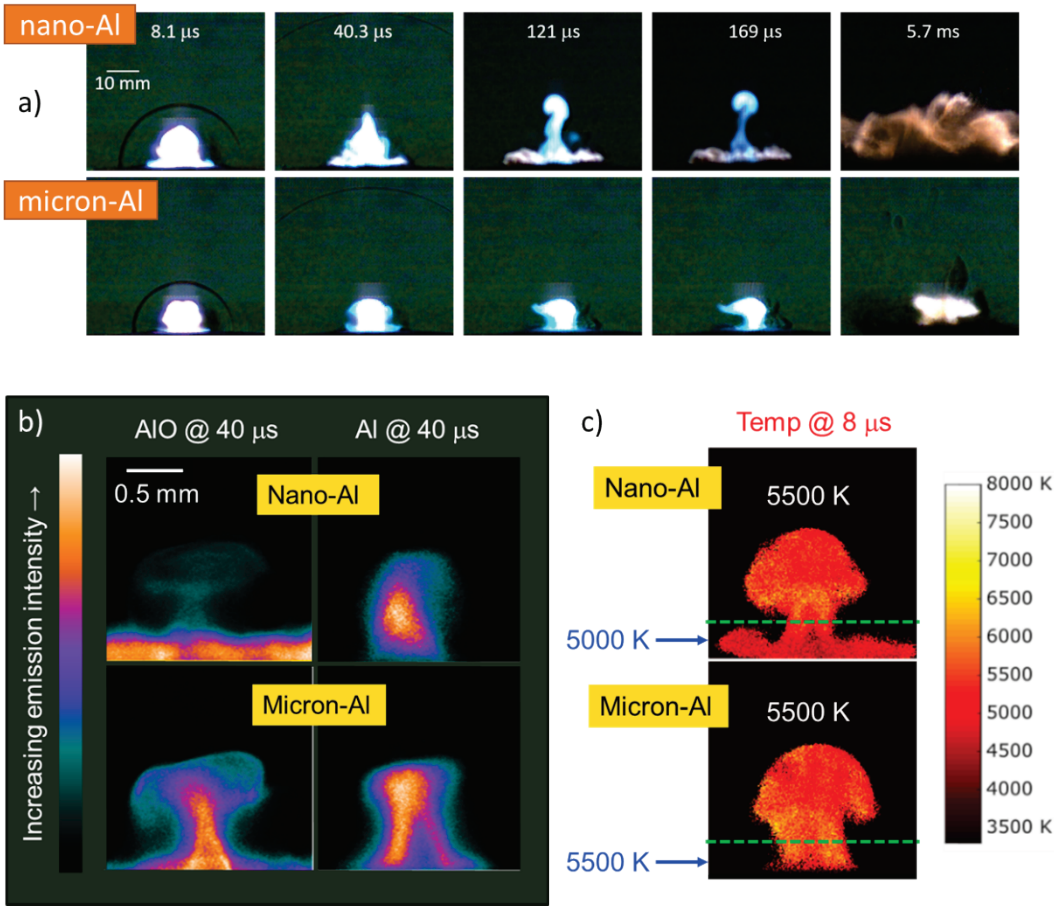

Fig. 2 Influence of aluminum morphology on a) combustion plume dynamics, b) species distribution, and c) plasma temperatures[8]

In this report, we continue to explore the differences in laser–material interaction resulting from particle size effects using the laser-induced air shock from energetic materials (LASEM) technique. LASEM is a laboratory-scale technique developed at the US Army Combat Capabilities Development Command (CCDC) Army Research Laboratory (ARL) to investigate the high-temperature chemical reactions of energetic materials subjected to rapid heating (~10^{13} K/s) via a nanosecond-pulsed laser.[9,10] Figure 3 shows a simplified cartoon of the events following pulsed laser excitation of an energetic material. The laser pulse is focused just below the sample surface, resulting in material ablation (typically several hundred micrograms per laser shot). The ablated material is rapidly ionized, forming a laser-induced microplasma and generating a laser-induced shock wave due to the temperature and pressure mismatch with the surrounding air. Under the LASEM conditions (laser pulse duration, energy, and wavelength), the plasma absorbs most of the energy in the laser pulse, that is, the absorption properties of the material have a negligible effect on the laser–material interaction. Following cessation of the laser pulse (after 6 nanoseconds [ns]), the plasma begins rapidly cooling and emission from atomic, ionic, and molecular species can be observed for approximately 15 µs. During this time, the laser-induced shock wave passes through the plasma region and is influenced by chemical reactions happening on the microsecond timescale. At later times, particles ejected from the sample surface pass through the air that has been heated by the plasma and the passage of the shock wave. For energetic materials, combustion reactions typically occur in the air above the sample on the timescale of tens of microseconds and/or tens of milliseconds.

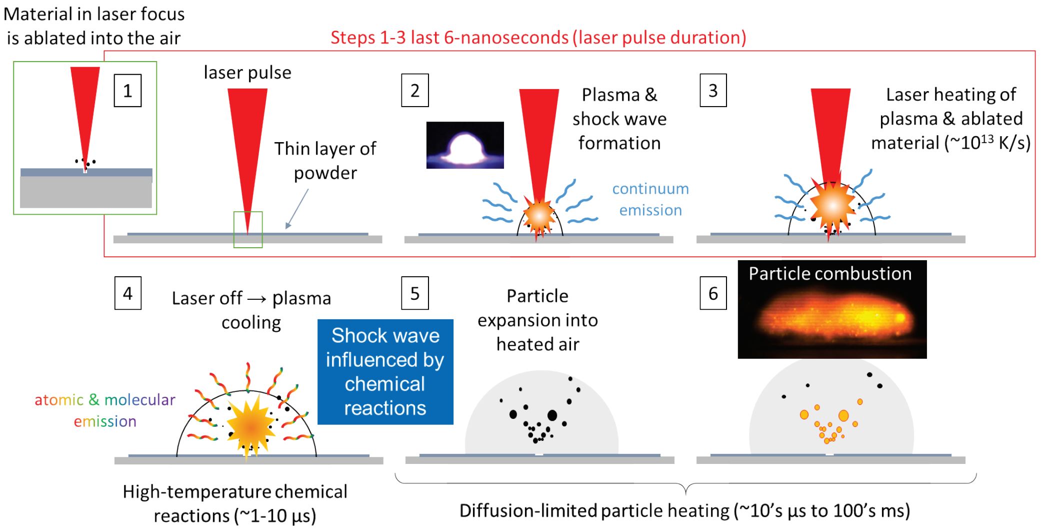

Fig. 3 **Simplified sequence of events following the pulsed-laser excitation of a thin layer of powdered sample that reacts exothermically when rapidly heated**

The timescales of material reactions following pulsed laser excitation (Fig. 3) can be roughly correlated to those pertaining to explosive effects following initiation of a detonation event (Fig. 4). At the earliest timescale (0–10 µs), the laser-induced shock velocities have directly correlated to the measured detonation velocities from large-scale testing of both conventional[10] and aluminized[11] military explosives. We have also shown correlations between the late-time combustion reactions observed with LASEM (1–200 ms) and blast effects from explosives.[11,12] For some materials, high-temperature combustion reactions immediately follow the plasma cooling (10–500 µs). We are currently investigating the relationship between combustion reactions in this time regime and the Gurney energy of an explosive.

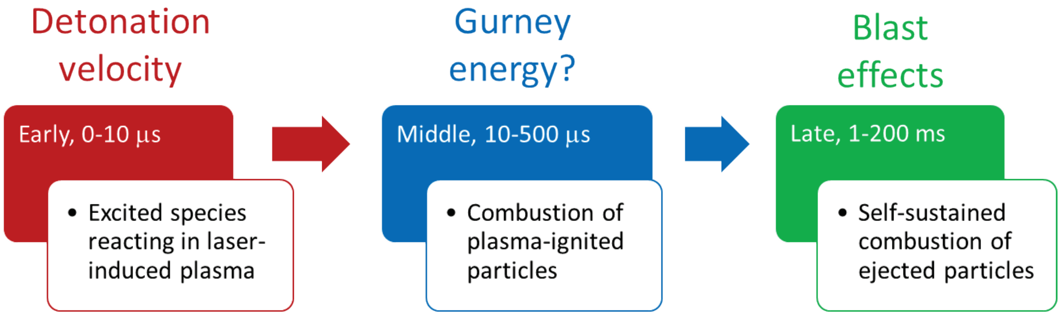

Fig. 4 **Time regimes following nanosecond-pulsed laser–material interaction and their relationship to the timescale of detonation effects**

Here, the time-resolution of the LASEM setup has been increased beyond that used in the original LASEM system[9,10] to improve the precision of the LASEM measurements. Several new diagnostic capabilities have also been added to the LASEM setup and are described here for the first time. Data on three Al samples acquired using this higher time-resolution LASEM setup have been used to investigate the influence of morphology on the chemical reactivity of laser-excited Al in air.

2. Experimental

2.1 LASEM Configuration

The basic configuration and example applications of LASEM have been previously described.[7,9–11,13–22] As before, a pulsed Nd:YAG laser (850 mJ, 6-ns pulse width, 1064 nm) was focused just below the sample surface to ablate, atomize, ionize and excite the material in the resulting laser-induced plasma. The propagation of the laser-induced shock wave into the air above the sample surface (through the plasma) was recorded using high-speed schlieren imaging. For this work, the high-speed camera (Photron FASTCAM SA5) was mounted on its side to increase the frame rate from 84,000 frames per second (fps) in the original LASEM setup to 420,000 fps in the current configuration (Fig. 5). Increasing the frame rate of the camera results in a decrease in the image size; by mounting the camera on its side, an image size of 832 × 16 pixels was obtained. This enabled us to track the propagation of the laser-induced shock wave into the air above the sample surface until it reached the top of the 4-inch-diameter schlieren mirror at a time-resolution of 2.38 μs between frames (compared to 11.9 μs at 648 × 64 pixels). In addition, the shutter exposure for the images was decreased from 1 μs to 369 ns to reduce saturation of the camera sensor by the laser-induced plasma emission at early times. All other components of the schlieren imaging setup remained the same as before (e.g., the use of a 200-W arc lamp as the light source and two 4-inch-diameter schlieren mirrors with a focal length of 45 cm). We collected high-speed video from 20 laser shots per sample. Multiple diagnostic methods for monitoring light emission from the laser-induced chemical reactions were added to the LASEM setup for the current study, as shown in Fig. 5 and described in Section 2.2.

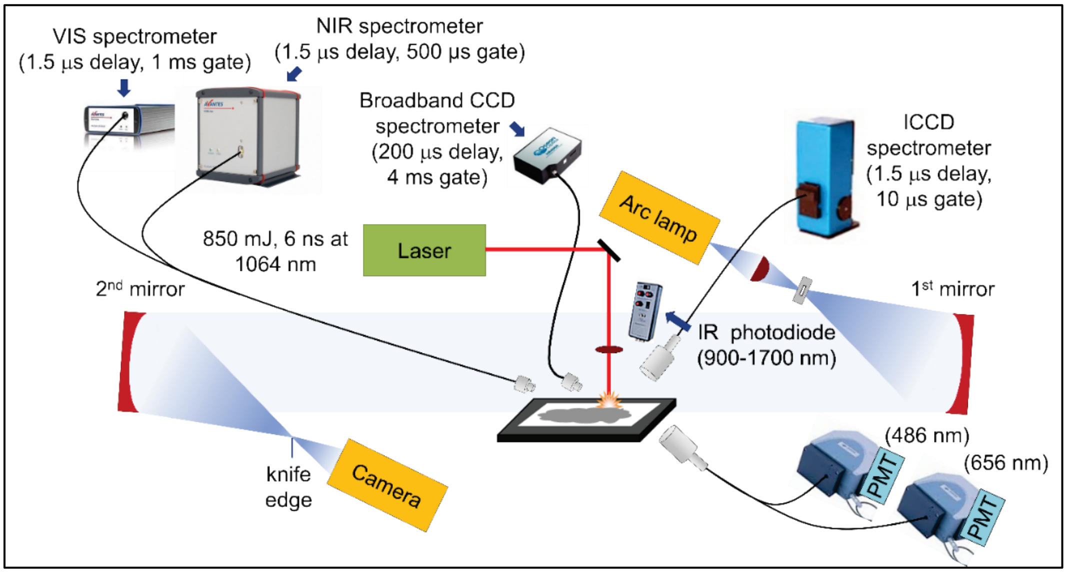

Fig. 5 Experimental schematic for the LASEM configuration used in this report. A z-type schlieren imaging system was used in conjunction with a high-speed color camera to record the propagation of the laser-induced shock wave into the air above the sample. Multiple spectrometers and detectors monitored the plasma and combustion emission at different time regimes.

2.2 Supplemental Diagnostic Methods

A digital delay generator (Stanford DG535) triggered by the Q-switch signal from the laser was used to control the gate delay and gate widths for the spectrometers described in the following sections. Signals from the photomultiplier tubes (PMTs) and the IR photoreceiver were recorded on an oscilloscope. A laptop was used to save the data from the high-speed camera, oscilloscope, and three spectrometers. A computer tower was used to save the data from a fourth spectrometer.

2.2.1 High-Resolution Plasma Emission Spectroscopy

An echelle spectrograph with an intensified charge-coupled device (ICCD) detector (Catalina Scientific SE200 with Apogee detector) was used to monitor the laser-induced plasma emission following laser excitation. The spectrometer has broad wavelength coverage from 200 to 1000 nm with an average resolution of 0.02 nm. The gain of the ICCD was set to 900, and the spectrometer trigger was delayed 1.5 μs after the laser fired to avoid the continuum emission. A gate width of 10 μs was selected to cover the duration of the shock wave passage through the plasma region. Spatially integrated light from the plasma was focused into the spectrometer's fiber-optic cable using an ultraviolet (UV)-collimating lens. Twenty single-shot spectra were saved for each sample.

2.2.2 Time-Resolved Aluminum Monoxide and Hydrogen Emission

Two matched Czerny-Turner spectrographs (Andor Shamrock) with PMT detectors (Thorlabs PMT1001) were intensity-calibrated with a tungsten-halogen light source (SLS201L). Spatially integrated light from the LASEM reaction region was collected with a collimating lens and focused into a bifurcated fiber-optic cable with an inline signal attenuator. The PMT gains for the Al samples were set to one, and data from a minimum of five laser shots were saved for each sample. The two monochromators were centered at 486.58 ±0.02 nm and 656.100 ±0.004 nm to monitor the time-resolved aluminum monoxide (AlO) and hydrogen (H) emission, respectively (Fig. 6). The signal from each monochomator/PMT was fit to a Voigt line profile to determine the full-width at half-maximum for each: 1.55 ±0.17 nm for the AlO line and 1.72 ±0.04 nm for the H line.

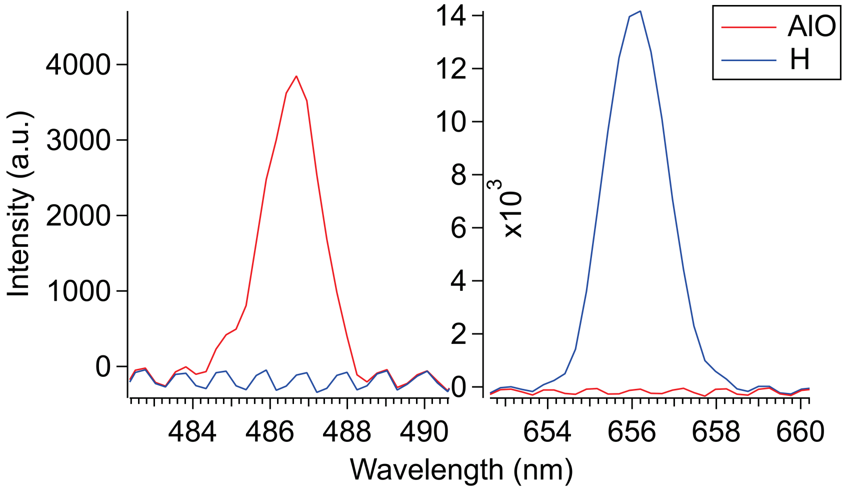

Fig. 6 Monochromator/PMT calibration images for AlO (left) and H (right) emission regions

2.2.3 Combustion Emission Spectroscopy

Emission spectra from the combustion of metal particles with air were obtained with a CCD spectrometer (Ocean Optics, HR4000) using a 200-µs gate delay to avoid the plasma emission and a 4-ms gate width. The spectrometer covers the wavelength region from 230–900 nm with a 0.25-nm resolution, and light from the combustion reactions was collected with a fiber-optic cable pointed at the interaction region. At least five single-shot spectra were saved for each sample.

2.2.4 Sequential Emission Spectra

Two additional spectrometers were used to obtain an automated series of 100 sequential emission spectra from each laser shot in the UV and visible (VIS) wavelength regions (Avantes, ULS2048) and near-infrared (NIR) region (Avantes, NIR512). The UV-VIS spectrometer had a wavelength range of 200 to 1100 nm with a 1.4-nm resolution. The first spectrum was delayed 1.5 µs, and each sequentially acquired spectrum had a 1.050-ms gate width. The NIR spectrometer had a wavelength range of 1000 to 2500 nm with an 8.9-nm resolution. The first spectrum was delayed 1.5 µs, and each sequentially acquired spectrum had a 500-µs gate width. The light for the two spectrometers was collected with two separate fiber-optic cables pointed toward the interaction region. The UV-VIS fiber-optic cable was placed more than a foot from the interaction region to avoid saturating the detector.

2.2.5 Integrated Infrared Emission

A free-space, 10-MHz IR-sensitive photoreceiver (New Focus Model 2053) was pointed at the combustion region. The integrated light emission (900–1700 nm) was saved for a minimum of five laser shots per sample. The gain was set to 3×10^2 for the Al plate and 3×10 for nano-Al and micron-Al.

2.3 Samples Sources and Preparation

Twenty laser shots were obtained for each of three Al samples. A 2-inch-square plate of Al alloy 2024 was directly ablated by the pulsed laser for analysis following a cleaning shot to remove surface contamination. Although precise specifications for this sample were not available, in general this alloy consists of 90.7%–94.7% Al, 3.8%–4.9% copper (Cu), 1.2%–1.8% magnesium (Mg), 0.3%–0.9% manganese (Mn), 0%–0.5% iron (Fe), 0%–0.5% silicon (Si), 0%–0.25% zinc (Zn), 0%–0.15% titanium (Ti), 0%–0.1% chromium (Cr), and less than 0.05% other metals. Micron-sized Al powder (micron-Al) specified as <75 µm (Sigma-Aldrich) was spread on double-sided tape affixed to a glass slide (~4.6 mg/cm^2). Based on 2-laser diffraction measurements,[22] the mean particle size for this sample is 28 ±15 µm. For comparison, an Al "nanopowder" sample from Sigma-Aldrich with a mean particle size of 110 ±2 nm (determined via dynamic light scattering[22]) was also prepared (nano-Al). The slide coverage for the nano-Al sample was approximately 2.3 mg/cm^2. Figure 7 shows the powder sample slides before and after laser ablation. Scorch marks from combustion of the Al in the air above the sample surface are visible for each sample. To ensure adequate spacing between laser shots, two sample slides were prepared for the nano-Al due to the significant blow-off region (i.e., particle scatter) following each laser shot.

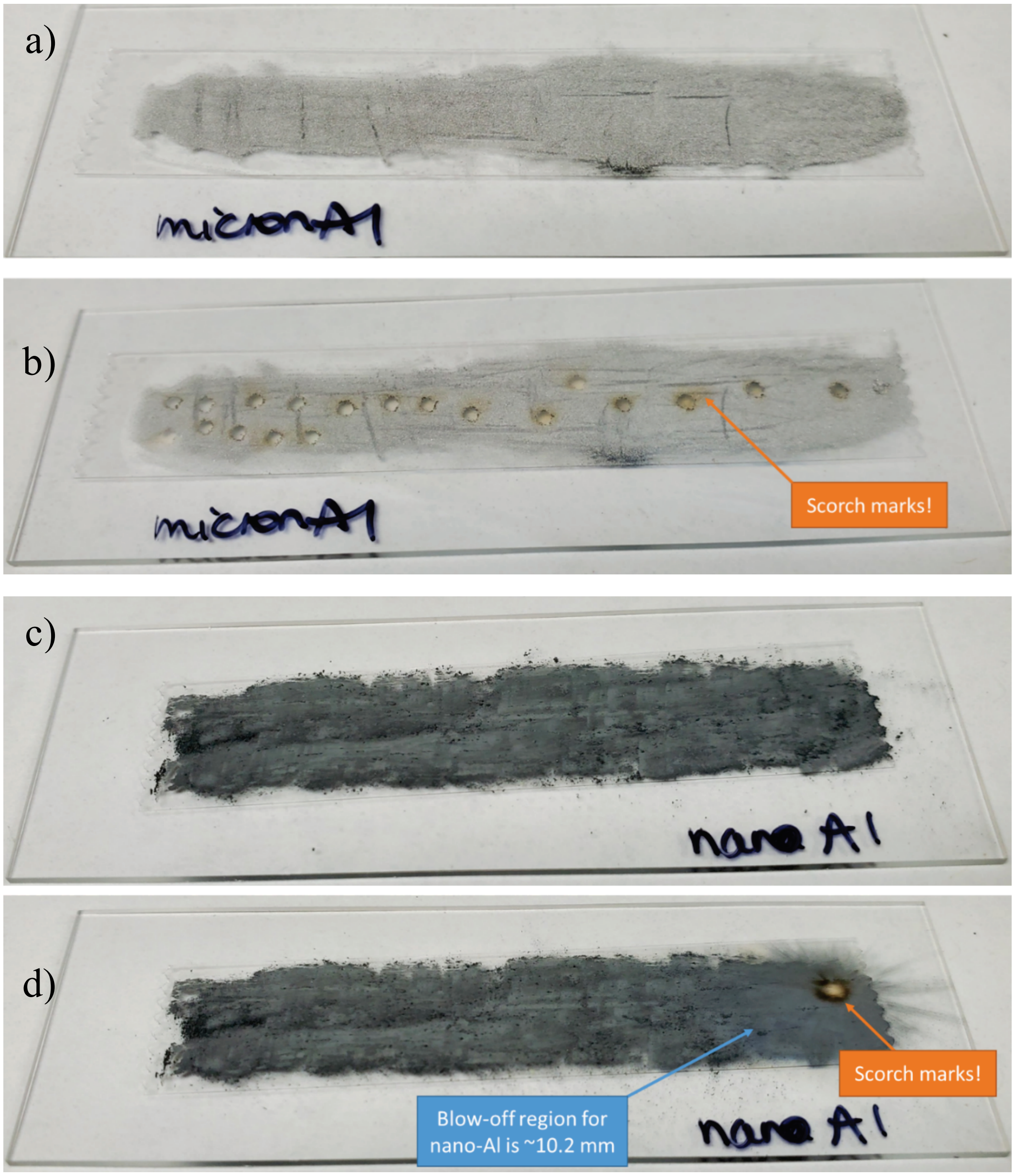

Fig. 7 Photographs of powder sample slides of micron-Al a) before and b) after 20 laser shots; and nano-Al c) before and d) after 1 laser shot

3. Results

3.1 High-Speed Imaging of Laser-Induced Shock Waves

Figure 8 shows select images from the high-speed video acquired following laser excitation of the Al samples. The images look very similar among the three samples, but differences include 1) an increase in plasma size and intensity where Al 2024 plate < micron-Al < nano-Al, 2) faster shock wave velocities at early times in the order Al 2024 plate ≤ micron-Al < nano-Al, and 3) the intensity of the AlO emission at 155 µs follows the order micron-Al > nano-Al > Al 2024 plate. The differences in shock wave position (above the sample surface) between sample types at each time step are measured to be fractions of a millimeter using custom MATLAB code (Fig. 9). Accurate measurement of the shock wave positions is thus critical for distinguishing samples based on the laser-induced shock waves. This is particularly challenging at early times when the plasma emission partially or completely obscures the shock wave (Fig. 8), resulting in larger confidence intervals at early times. We have found that automated edge-detection algorithms for determining the shock wave position at early times are insufficient for this application. For this data set, we used an edge-detection algorithm designed by Dr Brian Barnes (Army Research Laboratory) to determine the shock wave position once the shock wave exited the plasma region (i.e., after the first 7–10 frames); this algorithm will be described in more detail in Part II of this report series.[23] A custom MATLAB code was used to manually measure the shock wave positions at early times in a semi-automated method described previously.[9,10,15]

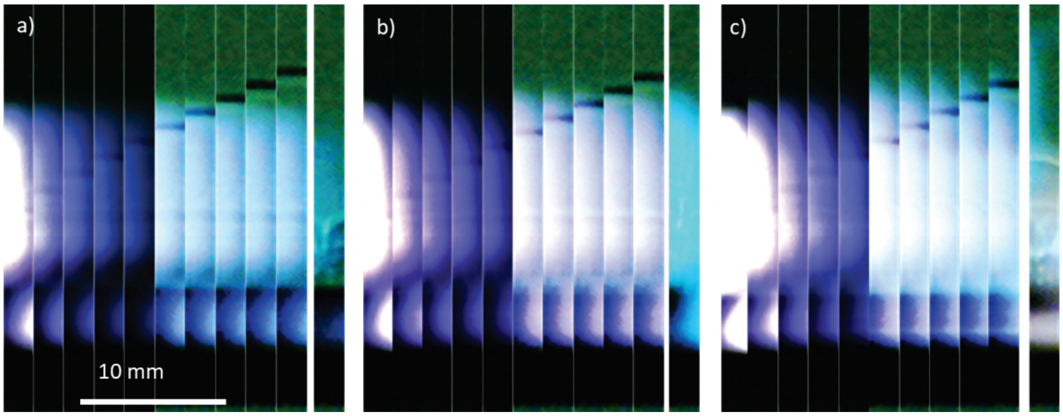

Fig. 8 Snapshots from the high-speed video acquired following laser excitation of a) an Al 2024 plate, b) micron-Al powder, and c) nano-Al powder. The first 10 frames cover the time from 0 to 23.8 µs and the last frame of each series is from 155 µs. All images have been cropped from the top, and the last six frames of each series were adjusted for brightness (+70%) and contrast (+20%).

By focusing on the time frame during which the laser-induced shock wave is propagating through the plasma region (and is thus affected by the chemical reactions that occur in the plasma), differences in the shock wave position as a function of time can be observed between the three Al samples (Fig. 9b). Due to the intense plasma emission from the nano-Al sample (Fig. 8c), the laser-induced shock wave could not be observed in the first frame for any of the laser shots. For the other two Al samples, strong plasma emission and jitter in the high-speed camera triggering resulted in relatively large error bars for the first shock wave positions (2.6% for the Al plate and 13% for the micron-Al powder). The nano-Al shock wave position appears to jump significantly at around 5 μs; however, the confidence intervals when the data from all 20 laser shots are averaged overlap, making it difficult to draw conclusions about the timing of the chemical reactions from the laser-induced shock wave positions. Shot-to-shot variations in the laser–material interaction are well-known to occur even for the pulsed laser ablation of inert materials due to the stochastic nature of the process. Even more significant shot-to-shot variation has been demonstrated for powdered materials (compared to bulk) and chemically reactive materials can increase the variability as well. For this reason, it is important to use high-speed imaging to record the propagation of the laser-induced shock wave into the air above the sample for the entire single-shot event. Averaging data obtained from multiple individual laser shots will significantly increase the measurement error and make it difficult to differentiate between samples based on the laser-induced shock velocity.

One way to improve the precision of the data fitting is to increase the time-resolution of the high-speed video.[15] Figure 10 compares the laser-induced shock wave position at three different camera settings for both powders. The data from the current study were acquired at 420,000 fps with a 369-ns exposure. The original LASEM setup used the same camera at a frame rate of 84,000 fps with a 1-μs exposure.[9,10] A separate LASEM-based setup used a monochrome camera (Photron SAZ) with a frame rate of 800,000 fps (159-ns exposure).[22] The measured shock wave positions depend on the camera settings as well as the laser parameters and sample type. The original LASEM time-resolution is not sufficient to accurately capture the early-time behavior of the laser-induced shock wave, although comparisons between different samples acquired under the same experimental conditions still show distinct differences.[9]

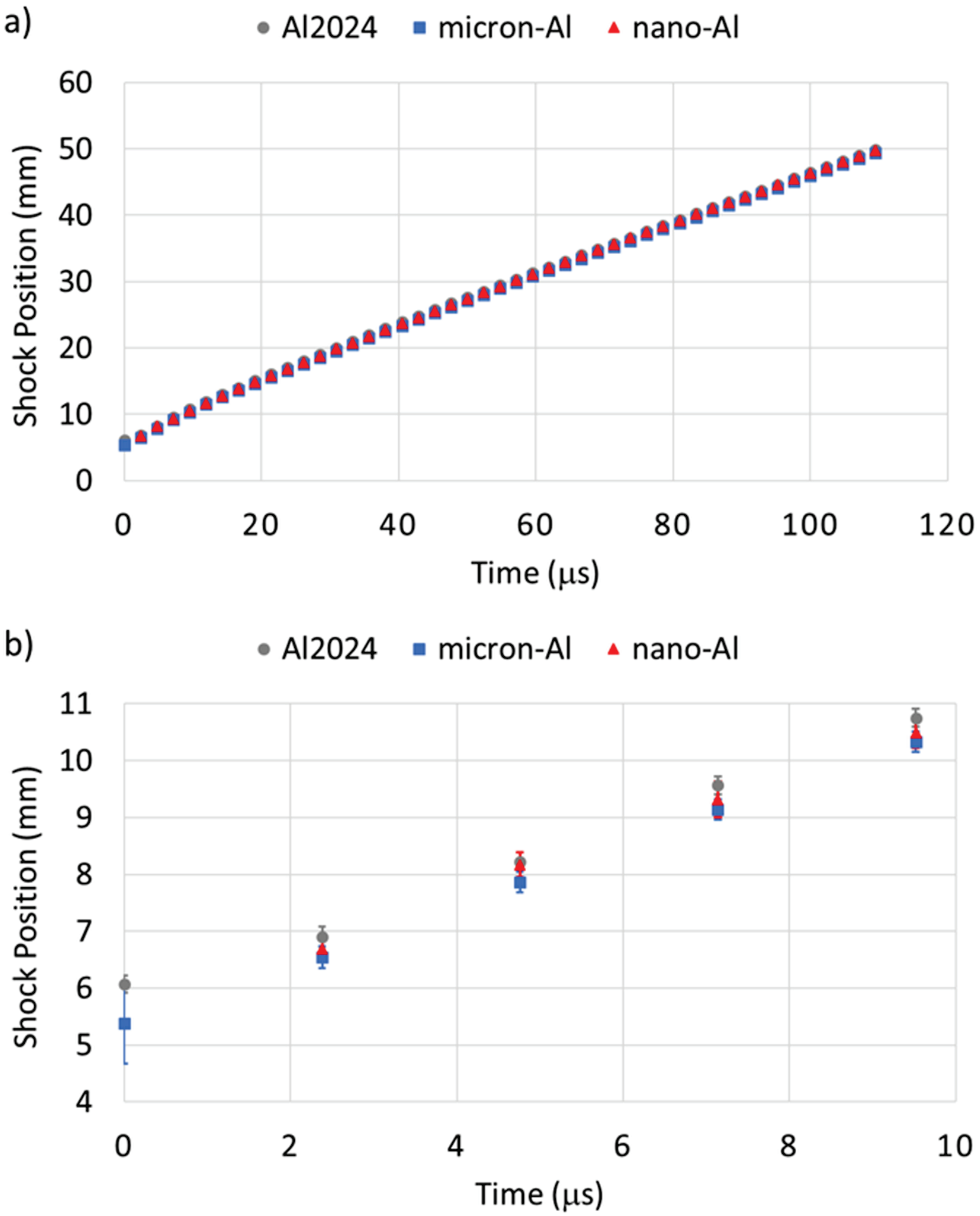

Fig. 9 Laser-induced shock wave position above the sample surface as a function of time for each of the three Al samples shown at a) full-scale and b) as the shock wave passed through the plasma region. Error bars are 95% confidence intervals.

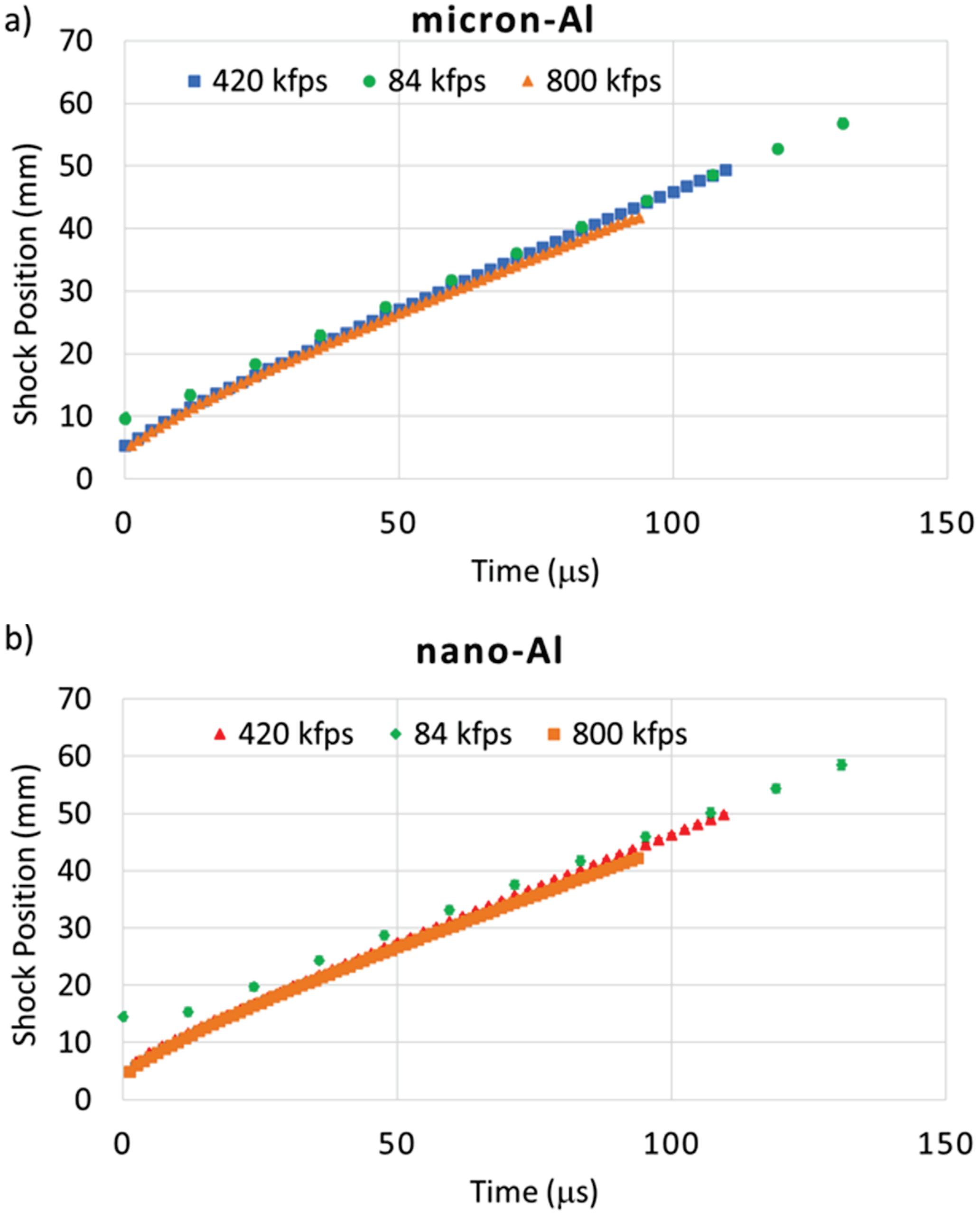

Fig. 10 Comparison of the laser-induced shock wave positions measured at three different high-speed camera settings for a) micron-Al and b) nano-Al. Error bars are 95% confidence intervals (too small to see at full-scale).

To compare the influence of the high-temperature chemistry in the laser-induced plasma on the laser-induced shock wave, we found that directly fitting the laser-induced shock velocities as a function of time using a fifth-order polynomial introduced the least amount of fitting error.[9] While it is possible to fit the shock position versus time and differentiate to obtain the shock velocity, this exacerbates the fitting error for the experimental data. This topic will be discussed in more detail in Part II of this report series.[23] Here, Fig. 11 shows the laser-induced velocities as a function of time for the three Al samples (data averaged over 20 laser shots for illustrative purposes). As before, the characteristic laser-induced shock velocity for a sample is defined as the y-intercept of the fifth-order polynomial fit to the data.[9] Figure 11a shows that this type of fit does not work as well for the higher time-resolution data as it did for the data collected at 84,000 fps (see, e.g., Gottfried 2014).[9] Here, the fit underpredicts the first data point for the nano-Al sample, and at later times when the laser-induced shock velocity decays to the speed of sound in air, the fit oscillates around the data points. This effect from polynomial interpolation is known as Runge's phenomenon and is more prominent for the most reactive samples (i.e., samples with the largest y-intercept).

Since the late-time data points contain little information about the sample, cutting off the data at 50 µs results in a more accurate polynomial fit similar to that obtained at 84,000 fps—without sacrificing fidelity of the data (Fig. 11b). The early data points are better represented by the fit and the Runge's phenomenon is minimized for the shock-wave decay to the speed of sound in air. It also results in a significantly higher characteristic laser-induced shock velocity for the nano-Al, emphasizing the more reactive nature of that sample on the microsecond timescale. For comparison purposes however, we fit the full-scale data for the three Al samples as shown in Fig. 11a to compare to previously collected data at different time resolutions using the same methodology (Fig. 11a, Table 1). Alternative fitting techniques will be explored in Part II of this report series.[23]

The data in Table 1 (and Fig. 12) demonstrate the consistency of the characteristic laser-induced shock velocities for the micron-Al and nano-Al samples determined using different LASEM setups. In all three cases, there is a clear difference in characteristic laser-induced shock velocities for micron-Al and nano-Al powders—indicating that more of the nano-Al is oxidized on the microsecond timescale. While the characteristic laser-induced shock velocities for bulk Al and micron-Al powder were similar, the influence of material hardness on the laser-induced shock wave under these conditions is not yet known. Previous studies suggested that an observed correlation between the extent of ionization in the laser-induced plasma and the material strength or hardness may be based on the strength of the reflection of the laser-induced shock wave off the sample surface.[24–26] In contrast to the bulk Al, for the Al powder samples the reflected shock wave transmits through the tape and glass slide before reflecting off the surface of the sample stage.

Table 1 also gives the characteristic laser-induced shock velocities that were determined by averaging the shock position data for all 20 laser shots for each sample prior to fitting the velocity versus time data. While in most cases the characteristic laser-induced shock velocities are similar to those averaged from the fits of individual laser shots, the averaged value for micron-Al is significantly lower —indicating shot-to-shot variations in the laser–material interaction and/or camera triggering influenced the averaged data.

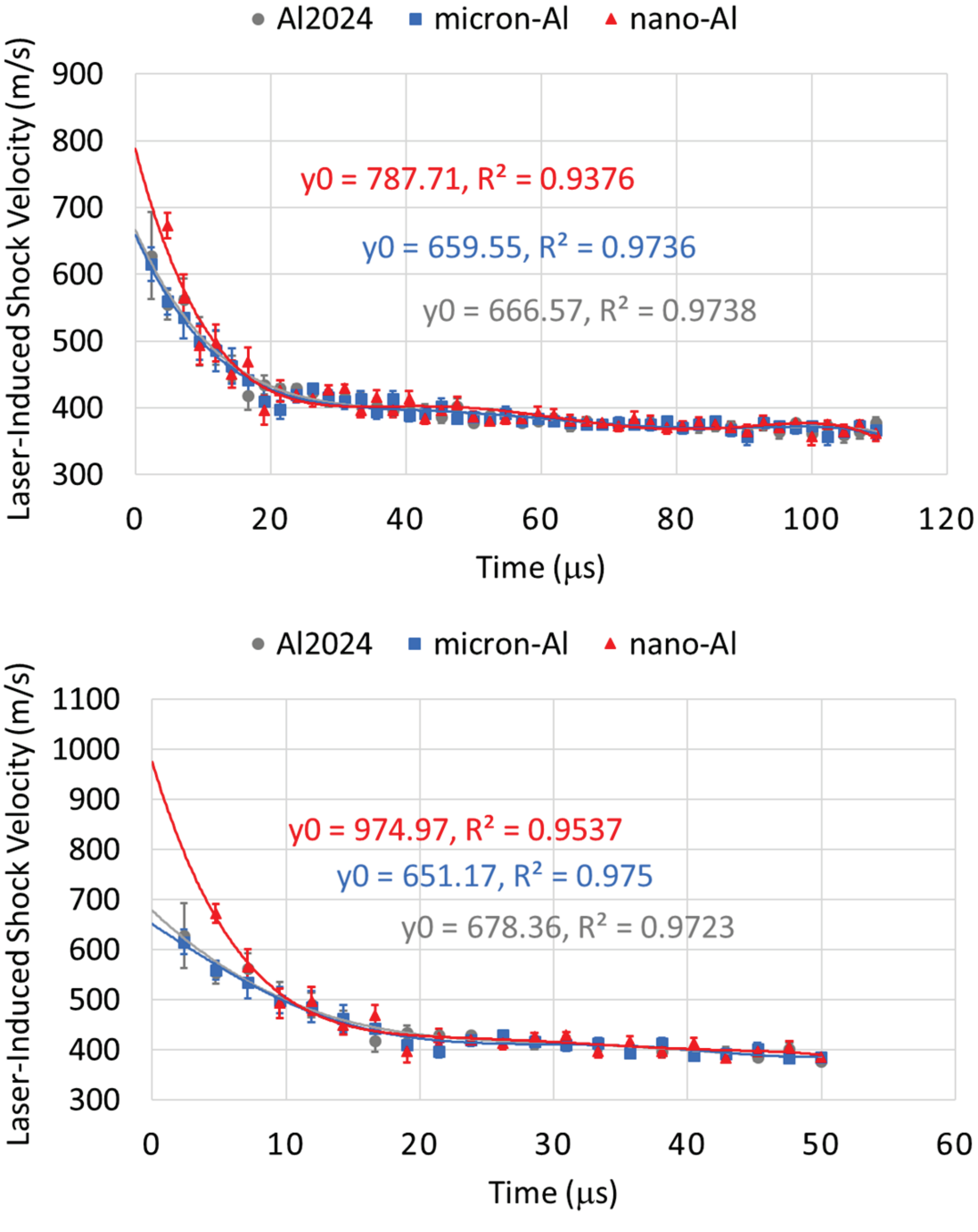

Fig. 11 Laser-induced shock velocities as a function of time for the three Al samples with fifth-order polynomial fits out to a) 110 μs (full-scale) and b) 50 μs (truncated data). The y-intercept and R-squared value for the quality of each fit are also shown.

Table 1 Characteristic laser-induced shock velocities for the three Al samples under different high-speed imaging settings

	Fit from averaged data			Fits from single-shot data					
Sample	**420 kfps (369 ns)**	**84 kfps (1 µs)**	**800 kfps (159 ns)**	**420 kfps (369 ns)**	**95% CI**	**84 kfps (1 µs)**	**95% CI**	**800 kfps (159 ns)**	**95% CI**
Al 2024	666.57	…	…	655.22	10.50	…	…	…	…
micron-Al	659.55	598.77	636.38	652.69	10.55	669.11	9.99	633.73	5.66
nano-Al	787.71	753.83	757.58	775.21	8.19	753.83	17.49	767.80	15.21

Note: CI = confidence interval.

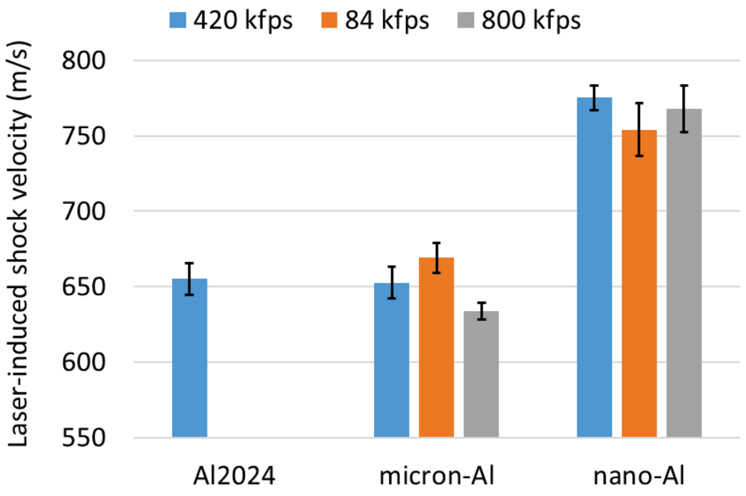

Fig. 12 Characteristic laser-induced shock velocities for the three Al samples under different high-speed imaging settings. Error bars are 95% confidence intervals.

3.2 High-Resolution Plasma Emission Spectroscopy

3.2.1 Shot-to-Shot Variation

As discussed previously, shot-to-shot variations in the laser–material interaction are common with pulsed laser ablation. In addition to affecting the confidence intervals for the laser-induced shock velocities, shot-to-shot variations in the laser-induced plasma emission intensities also occur (Fig. 13). The relative standard deviations (RSDs) of atomic, ionic, and molecular emission intensities vary from approximately 10% to 80% depending on the species and sample. Since entrainment of air into the plasma contributes significantly to the oxygen (O) and N emission features, their RSDs are generally less than 10%. The data points for each spectrum in Fig. 13 were plotted as individual markers for easier comparison to the average spectrum. Note that the single-shot spectra were acquired from the same laser shots used to evaluate the propagation of the laser-induced shock velocities each sample, as described in Section 3.1.

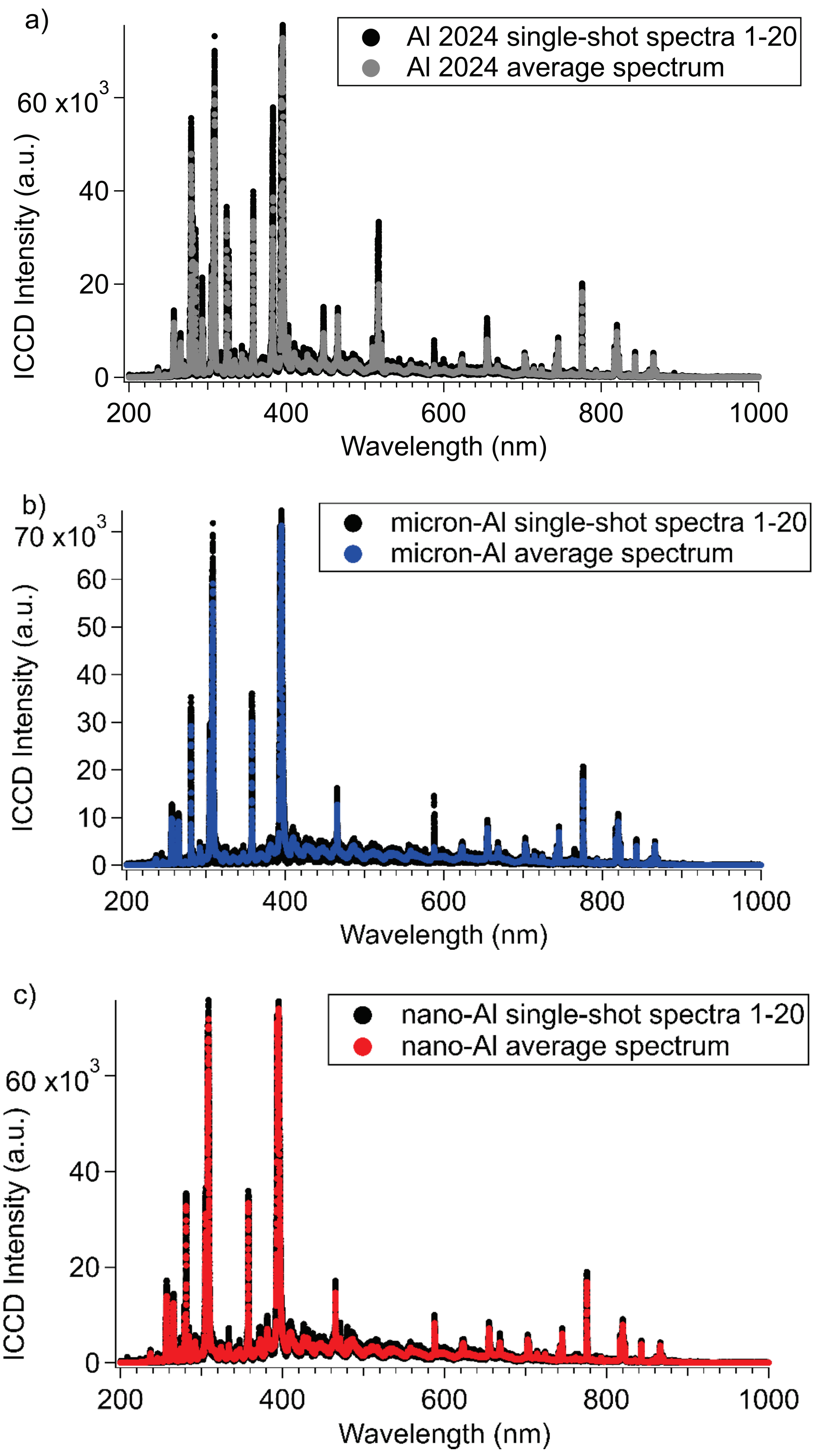

Fig. 13 **Single-shot and average spectra of a) an Al 2024 plate, b) micron-Al powder, and c) nano-Al powder**

3.2.2 Sample Composition

Figure 14 shows the average plasma emission spectra for the three Al samples. Major emission features are labelled and consist of species due to the Al (Al I, Al II, and AlO), metal impurities (Fe, Si, Li, Mg, Ti, etc.) and organic species (C, H, N, O, and CN). Figure 15 compares the emission intensities of each species detected in the Al samples, as well as some emission ratios of interest. Error bars consist of 95% confidence intervals. In addition to species concentration, emission intensities are influenced by the transition strength for the particular emission feature and the temperature. However, at the extremely high plasma temperatures (which drop from ~14,500 to ~9,500 K between 1 and 11 µs),[8] differences in plasma temperatures do not significantly affect the emission intensities (compared to combustion temperatures on the order of a few thousand kelvin).

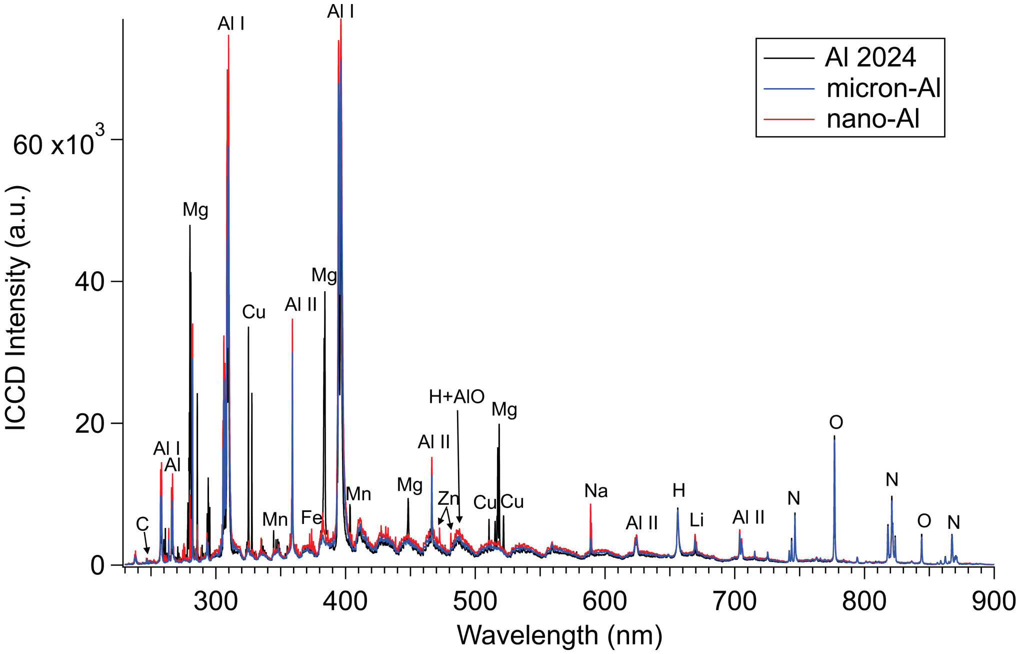

Fig. 14 Laser-induced plasma spectra for bulk Al, micron-Al powder, and nano-Al powder (average of 20 spectra each)

While the bulk Al alloy contains other metal species as expected (Section 2.3), both Al powders also contain trace amounts of metal impurities—particularly the nano-Al. The powders also contain more organic material (Fig. 15b), most likely as functional groups on the alumina shell although there may also be some contribution from organic impurities mixed in with the particles. The rapid heating of nano-Al generates more AlO in the laser-induced plasma due to the higher specific surface area and reactivity with the available O from ablated material and entrained air. Obtaining accurate emission intensities for the AlO emission in the laser-induced plasma is challenging because the strongest features are convoluted with the broad H_β emission line at 486 nm. On the other hand, the H emission is lowest for the nano-Al sample (Fig. 15a), which supports the observation of stronger AlO emission. As we previously observed for Al samples,[8] both the plasma temperature and ionization drop more rapidly the more reactive the sample is; thus, the ionization ratio is lower for nano-Al than micron-Al (Fig. 15c). The O/N ratio is highest for nano-Al—presumably due to the higher relative concentration of O from the alumina shell in each particle, that is, the active Al content of micron-Al is significantly higher (Fig. 1).

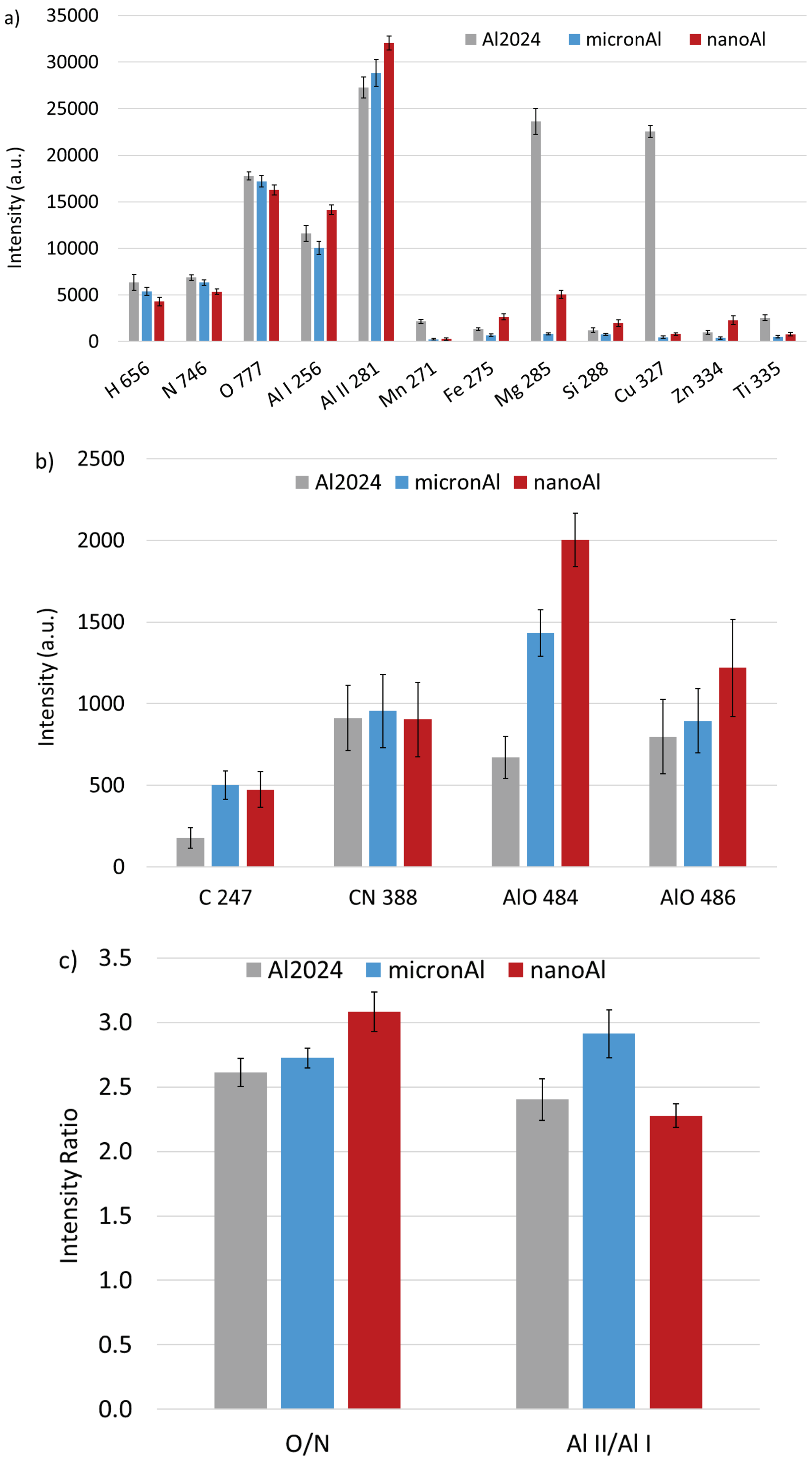

Fig. 15 **Comparison of the laser-induced plasma emission intensities (a, b) and ratios (c) for the Al samples. The numbers following the species name indicate the approximate wavelength of the emission feature (in nanometers).**

3.3 Time-Resolved AlO and H Emission

The time-resolved emission intensity from the monochromator/PMT set to monitor the H line shows that the H intensity in the laser-induced plasma followed the trend Al 2024 > micron-Al > nano-Al (not shown), which agrees with the integrated H emission trend shown in Fig. 15a. The only other signal from the H PMT was a very small peak in intensity near 1 ms for the nano-Al, which was due to gray-body emission from combusting particles rather than H emission; no atomic/ionic species emission is observed from the laser-induced plasma after approximately 15 µs. This spike in combustion emission corresponds to an increase in AlO emission, as shown in Fig. 16b and confirmed previously[22] via time-resolved emission spectroscopy.

At times less than 1 ms (the intermediate time regime described in Fig. 4 and shown in Fig. 16c), the time to postplasma AlO emission peak follows the order nano-Al < micron-Al < bulk Al. In this regime, we hypothesize that the observed emission comes from particles ejected off the sample surface being ignited by the hot gases present immediately following the laser-induced plasma dissipation (Fig. 17).[8] The Al powder samples exhibit more combustion emission on the combustion timescales (intermediate and late time) because more particles are ejected off the sample surface by the laser-induced shock wave and its reflections. Since the ignition temperature decreases with decreasing particle size, this suggests most of the particles ablated from the bulk Al sample that combust in this regime are larger than the average 28-µm particles from the micron-Al. Any small Al nanoparticles ablated from the Al plate by the pulsed laser (typically 10–20 nm in size based on other laser ablation experiments[4–7]) would have already reacted in the laser-induced plasma, generating the AlO emission seen in the integrated emission spectra (Fig. 15b) and in Fig. 16d. Note that at very early times (less than ~6 µs), continuum emission from the plasma saturates the PMTs.

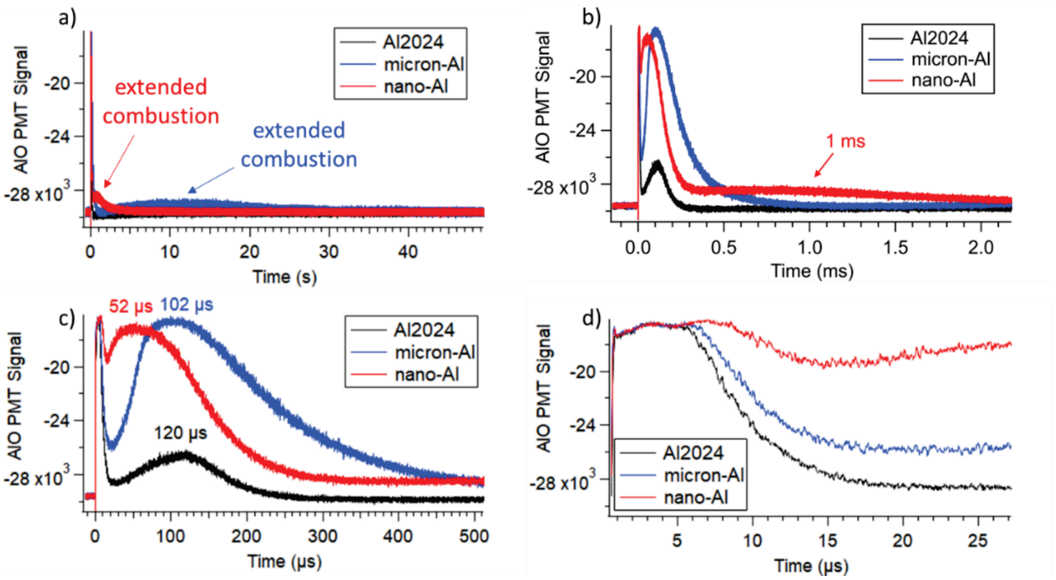

Fig. 16 Time-resolved AlO emission for the Al samples; parts a–d show the same data on different timescales

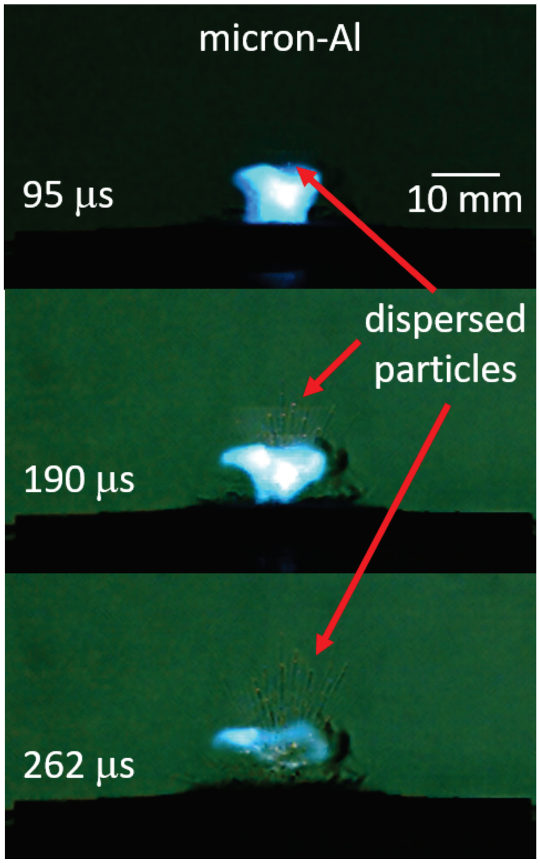

Fig. 17 High-speed video snapshots of micron-Al particles dispersing away from the substrate and combusting in a hot region of air and vaporized material.[8] The blue emission is from AlO.

3.4 Integrated Infrared Emission

On the late-combustion timescale (relevant for blast effects [Fig. 4]), particles ejected off the sample surface enter the region of air previously heated by the laser-induced plasma, the passage of the laser-induced shock wave, and any earlier combustion reactions. For most energetic materials, this results in a cloud of combusting particles above the sample surface (Fig. 18).[12] The time-to-peak combustion and combustion duration in this regime depends on the sample properties (ignition temperature, environmental temperature based on early exothermic reactions, etc.). While laser ablation of bulk Al does not result in significant combustion emission on an extended timescale, the time-to-peak combustion and combustion duration are significantly shorter for nano-Al compared to micron-Al (Fig. 19). The intensity of the combustion and the size of the combustion cloud depends on the sample preparation, that is, the number of particles ejected into the air above the sample surface.[17]

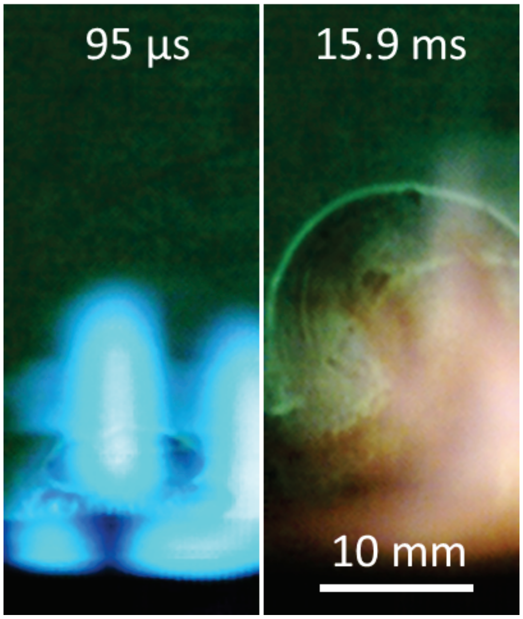

Fig. 18 High-speed video snapshot of micron-Al particles combusting 15.9 ms after the pulse laser excitation (the image at 95 µs from the same laser shot is shown for comparison). Most of the combustion cloud is out of the camera's field of view (which is focused in front of the laser–material interaction region to emphasize the shock-wave propagation at early times); the brightness (+50%) and contrast (+20%) were increased for both images. The blue emission (left) is from AlO and the orange emission (right) is primarily from excited Na atoms.

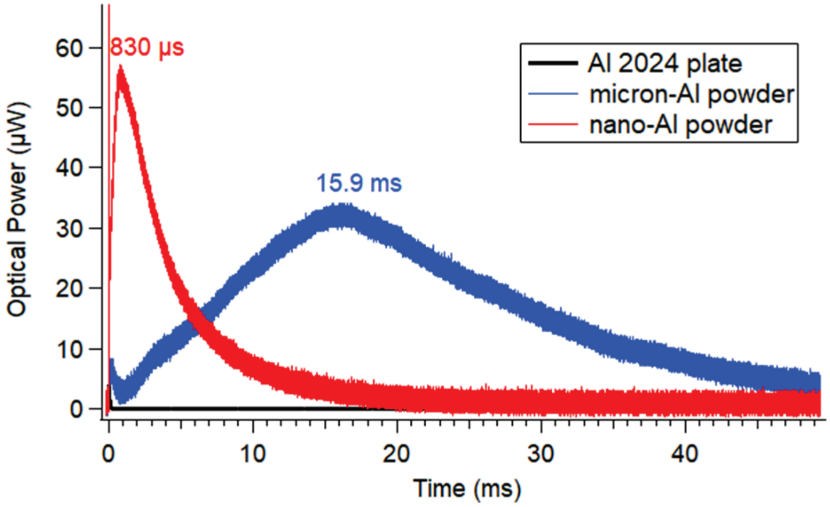

Fig. 19 Time-resolved integrated IR emission for the Al samples. The initial spike at time zero is due to the laser-induced plasma.

3.5 Combustion Emission Spectroscopy

The emission spectra from the late-time combustion are shown in Fig. 20. Because the combustion region is at much-lower temperatures than the plasma region, the spectra are dominated by gray-body emission from the burning particles and molecular emission. While a few atomic emission features were observed (Al, Fe, Na, Ca, H, and O), no ionic emission appears in the combustion spectra. It is important to note that the micron-Al powder generated significant combustion on this timescale (Fig. 19), which saturated the spectrometer for every laser shot except for the one shown in Fig. 20, which was acquired after most of the material had been ejected from the sample slide.

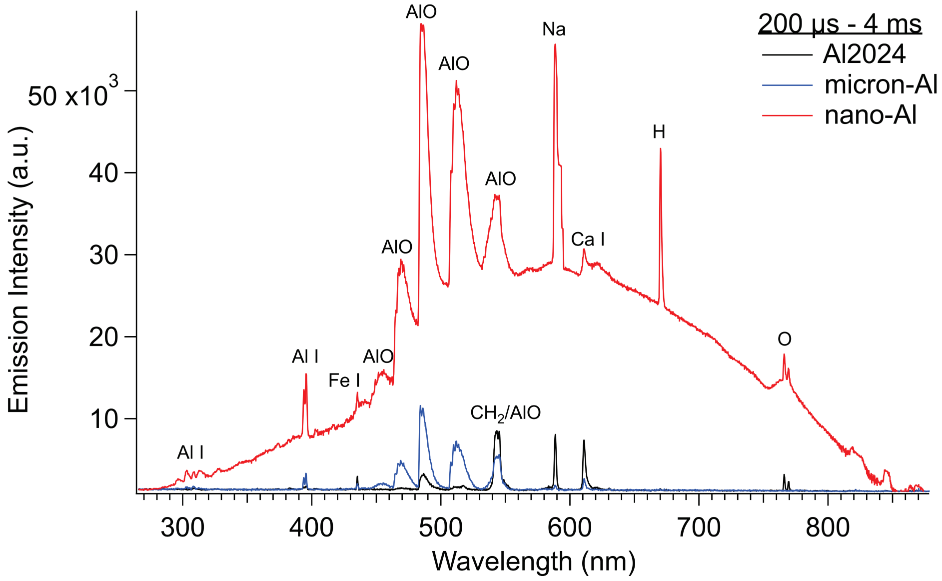

Fig. 20 Combustion emission spectra for the Al samples integrated from 200 µs to 4 ms after the pulsed laser excitation. Broadband gray-body emission and molecular emission dominate the spectra in this regime. While the spectra for nano-Al and the Al plate are averaged over multiple laser shots, most of the micron-Al spectra completely saturated the spectrometer and had to be discarded (only the single-shot spectrum shown in blue was usable). Thus, the gray-body emission for micron-Al is actually significantly stronger than that of nano-Al on this timescale.

3.6 Sequential Emission Spectra

Additional spectra were acquired using a fiber-optic cable placed much farther from the reaction region to avoid saturating the spectrometer. A series of 100 spectra were sequentially acquired following each laser pulse, as shown in Fig. 21. These data confirm the longer-lived combustion emission observed for the micron-Al compared to nano-Al (Fig. 19) and the increased combustion intensity for the powdered samples compared to the bulk sample.

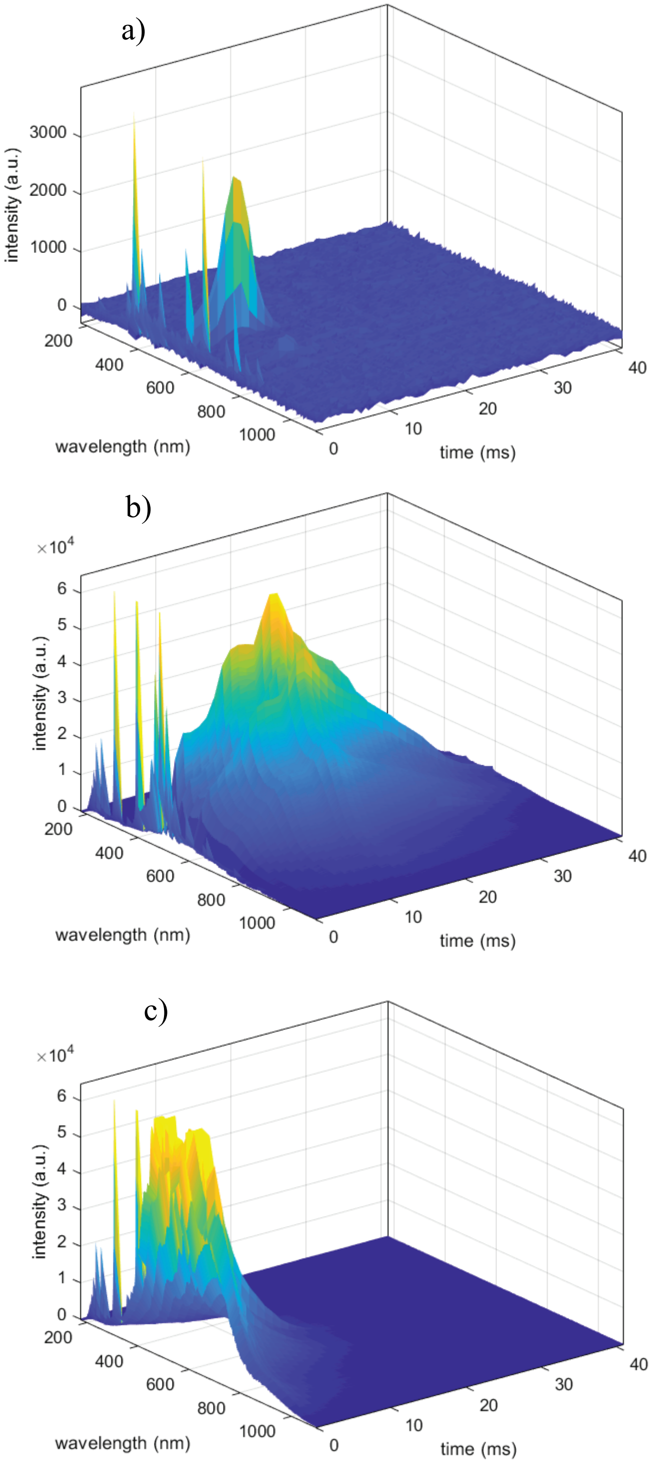

Fig. 21 **Sequential visible emission spectra acquired following pulsed laser excitation of a) bulk Al 2024, b) micron-Al, and c) nano-Al powder (representative series for each sample shown)**

For direct comparison of the emission spectra between samples, Fig. 22 shows the first (delayed by 1.5 μs after the laser pulse) and fifth spectra from each series. At longer times, ionic emission features rapidly disappear, atomic emission decreases, and gray-body emission increases. Figure 23 shows the background-corrected, time-resolved emission from a) atomic Al, b) atomic O, and c) AlO during the late-time combustion of the three Al samples. Note the logarithmic y-axis for the atomic emission. While emission from the nano-Al consistently decays over the first 20 ms, the emission from micron-Al decays exponentially, then peaks again around 15 ms. The bulk Al 2024 sample does not significantly combust or emit in this time regime.

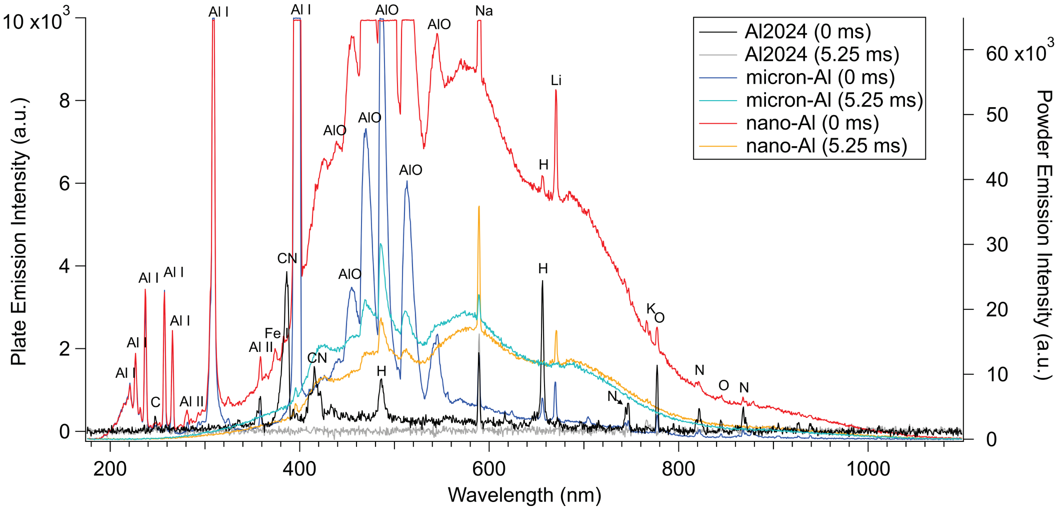

Fig. 22 **Selected spectra from the sequentially obtained series of visible emission spectra for the three Al samples**

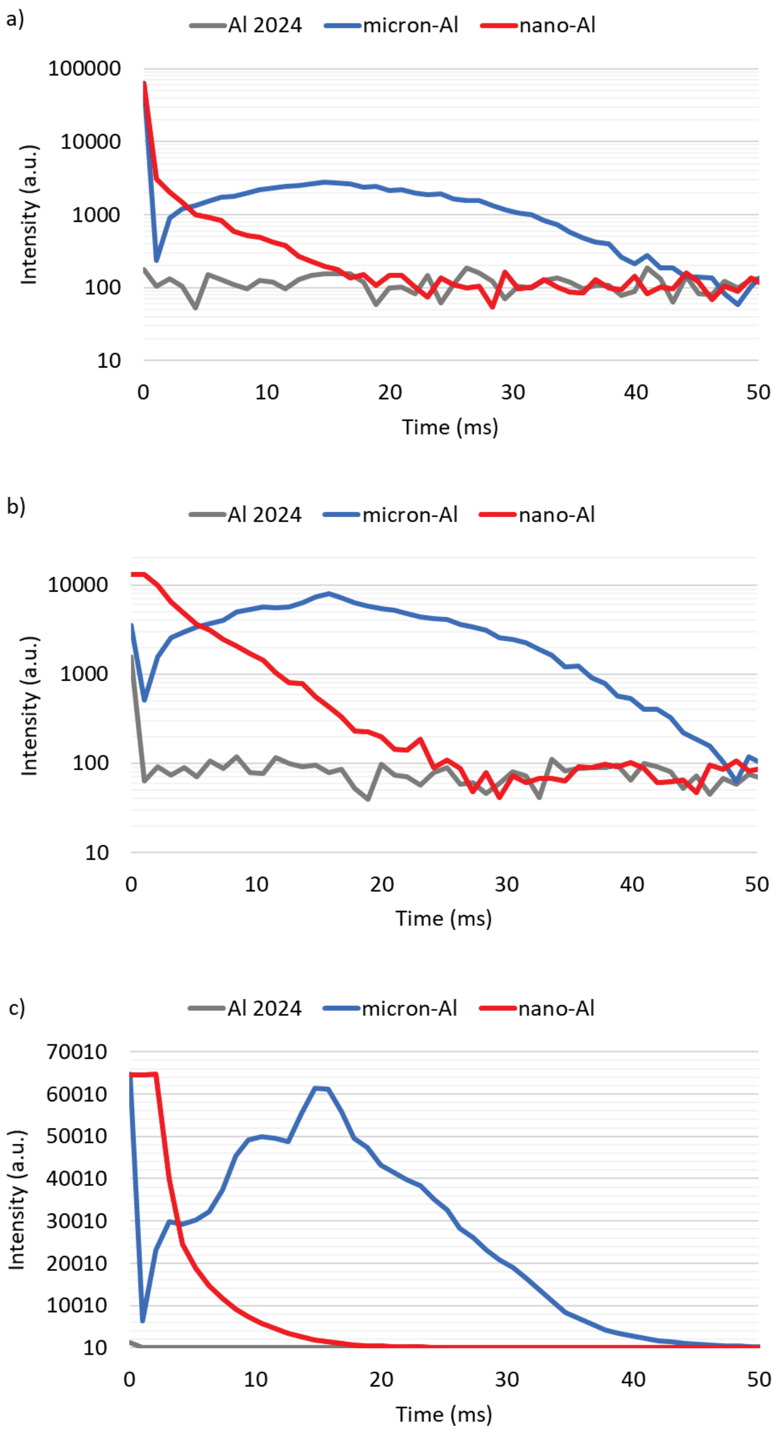

Fig. 23 **Time-resolved emission from a) Al I (308/309 nm), b) O (777 nm), and c) AlO (484 nm) from the sequential combustion spectra of the three Al samples**

The sequential NIR spectra for the three Al samples are shown in Fig. 24. Emission features in this region typically consist of vibrational overtone and combination bands from species such as H_2O, R-OH, and $-CH_x$. Figure 25 shows selected emission spectra from the spectral series, including tentative feature assignments based on those given in Zapata et al.[27] The spectra in Fig. 25 have been corrected for the spectral response of the spectrometer. Surprisingly, there is no evidence for atomic emission species such as Al, O, Na, or K—even at the earliest times. However, the relatively long gate duration for each spectrum (500 µs) might result in stronger vibrational features obscuring any atomic emission features that disappear rapidly as the plasma cools. The first spectrum in each sample series only differs in intensity compared to later spectra. Al I lines at 1312 and 1315 nm were observed in Koch et al. following detonation of PETN with 5% Al, but their emission lasted less than 21 µs.[28] Here, these lines were not present in the Al plate spectrum (Fig. 25), so they are probably not present in the Al powder spectra either. The vibrational features are presumably due to organic surface functional groups. Based on the laser-induced plasma emission spectra (Fig. 15), the Al plate has the most intense H emission, but commercial Al particles have more C; due to its larger specific surface area, nano-Al is expected to have more surface functional groups than micron-Al. The stronger intensity of the vibrational bands for the micron-Al could be a result of more combusting particles being present in this time regime. Because obtaining NIR spectra of laser-excited species is a new capability in our laboratory (and is generally quite uncommon for these types of samples), we still have much to learn about the observed spectral features in this region. Part II will discuss the assignment of NIR features for energetic materials in more detail,[23] and Part III will explore the effect of adding Al to energetic materials on the NIR spectra.[29]

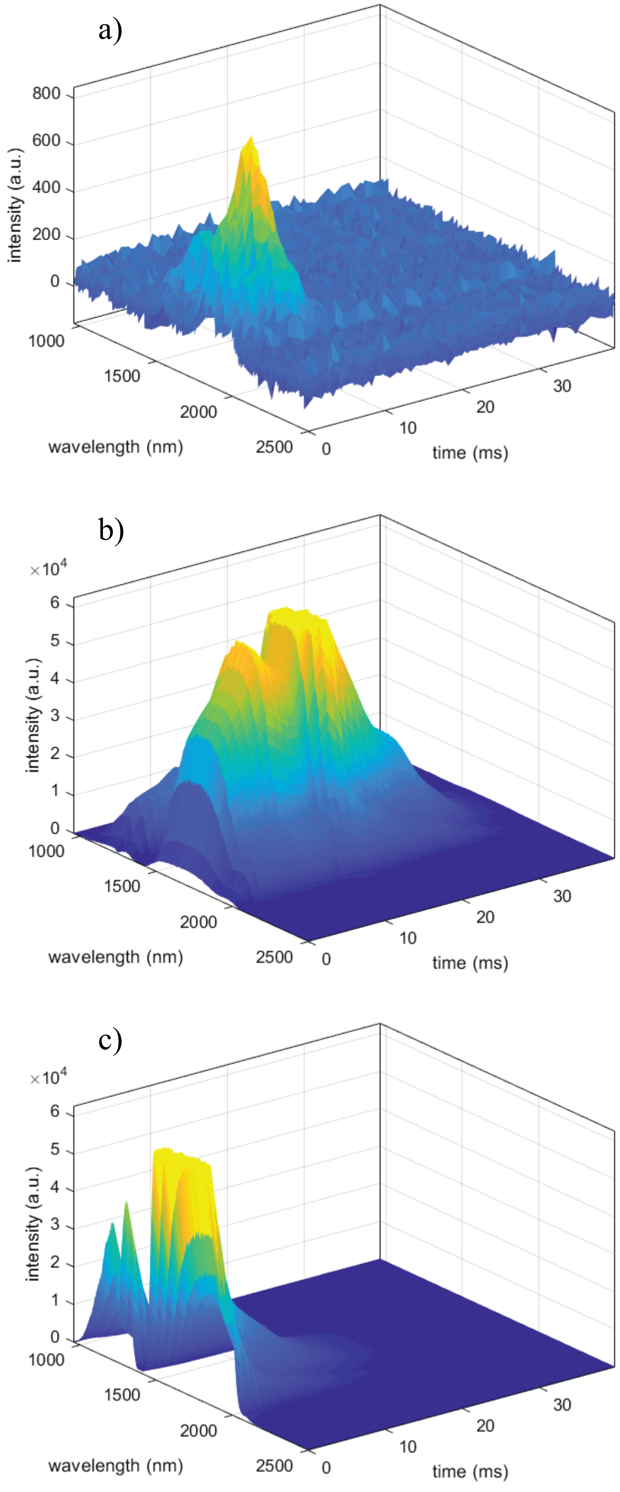

Fig. 24 Sequential NIR emission spectra acquired following pulsed laser excitation of a) bulk Al 2024, b) micron-Al, and c) nano-Al powder (representative series for each sample shown)

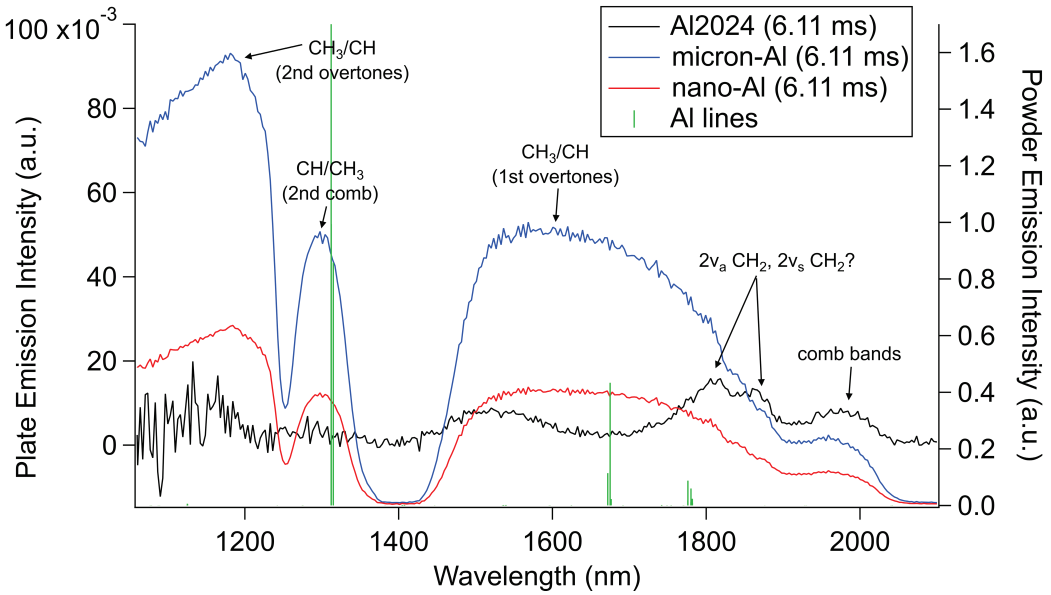

Fig. 25 Selected intensity-corrected spectra from the sequentially obtained series of NIR emission spectra for the three Al samples

4. Conclusions

In Part I of this report series we have demonstrated differences in energy release rates and high-temperature Al chemistry resulting from morphological differences using a new LASEM setup with improved time-resolution and diagnostic capabilities. The results from this work include the following:

- A comparison of characteristic laser-induced shock velocities from three different LASEM configurations confirms that nano-Al releases more energy on the microsecond timescale than micron-Al.
    - ○ This result was also supported by the increase in AlO emission on the microsecond timescale for nano-Al compared to micron-Al (and the bulk Al plate), as measured by both gated plasma emission spectroscopy and a time-resolved monochromator/PMT detector.
- A fifth-order polynomial fit underpredicts the early laser-induced shock velocities in the higher time-resolution data and exhibits Runge's phenomenon, unlike the original LASEM data used to correlate laser-induced shock velocities to measured detonation velocities from large-scale testing of explosives.
- On an intermediate timescale following cessation of the laser-induced plasma, the time-to-peak AlO emission and combustion shows the trend

nano-Al < micron-Al < Al plate, which follows the expected trend in ignition temperature.

  - This same trend in time-to-peak AlO/combustion emission was observed for late-time combustion on the millisecond timescale; however, the Al plate did not significantly combust in this time regime.

- NIR emission spectra of laser-excited bulk and powdered Al were observed for the first time; tentative assignments suggest that vibrational features dominate atomic features in this region.

Part II of this report series will present data from five different conventional military explosives collected with the upgraded LASEM system described in this report.[23] Alternative methods for data fitting will be discussed and the correlation between the characteristic laser-induced shock velocities and measured detonation velocities from large-scale testing will be evaluated. Part III of this report series will focus on the differences in energy release rates and chemistry observed when nano-Al powder was mixed in with two different explosives.[29]

5. References

1. Cremers DA, Radziemski LJ. Handbook of laser-induced breakdown spectroscopy. 2nd ed. Singapore: John Wiley & Sons, Ltd.; 2013.
2. Gottfried JL. Laser-induced breakdown spectroscopy. 2nd ed. Singh J, Thakur S, editors. Amsterdam (Netherlands): Elsevier Science; 2020. Chapter 12, Defense applications.
3. Yetter, RA, Risha GA, Son SF. Metal particle combustion and nanotechnology. Proc Combust Inst. 2009;32(2):1819–1838.
4. Gottfried JL. Laser-induced plasma chemistry of the explosive RDX with various metallic nanoparticles. Appl Opt. 2012;51(7):B13–B21.
5. Baldai A, Mamoory RS. Investigation of different liquid media and ablation times on pulsed laser ablation synthesis of aluminum nanoparticles. Appl Surf Sci. 2010;256(24):7559–7564.
6. Crouse CA, Shin E, Murray PT, Spowart JE. Solution assisted laser ablation synthesis of discrete aluminum nanoparticles. Mater Lett. 2010;64(3):271–274.
7. Davari SA, Gottfried JL, Liu C, Ribeiro EL, Duscher G, Mukherjee D. Graphitic-coated Al nanoparticles manufactured as superior energetic materials via laser ablation synthesis in organic solvents. Appl Surf Sci. 2019;473:156–163.
8. Wainwright ER, Dean SW, De Lucia FC Jr, Weihs TP, Gottfried JL. Effect of sample morphology on the spectral and spatiotemporal characteristics of laser-induced plasmas from aluminum. Appl Phys A. 2020;126(2):83.
9. Gottfried JL. Influence of exothermic chemical reactions on laser-induced shock waves. Phys Chem Chem Phys. 2014;16:21452–21466.
10. Gottfried JL. Laboratory-scale method for estimating explosive performance from laser-induced shock waves. Propellants Explos Pyrotech. 2015;40(5):674–681.
11. Gottfried JL, Bukowski EJ. Laser-shocked energetic materials with metal additives: evaluation of chemistry and detonation performance. Appl Opt. 2017;56(3):B47–B57.
12. Collins ES, Gottfried JL. Laser-induced deflagration for the characterization of energetic materials. Propellants Explos Pyrotech. 2017;42(6):592–602.

13. Gottfried JL, Klapötke TM, Witkowski TG. Estimated detonation velocities for TKX-50, MAD-X1, BDNAPM, BTNPM, TKX-55 and DAAF using the laser-induced air shock from energetic materials technique. Propellants Explos Pyrotech. 2017;42:353–359.

14. Gottfried JL, Dean SW, Collins ES, Collins C-C. Estimating the relative energy content of reactive materials using nanosecond-pulsed laser ablation. MRS Adv. 2018;3(17):875–886.

15. Gottfried JL. Laser-induced air shock from energetic materials (LASEM) method for estimating detonation performance: challenges, successes and limitations. AIP Conf Proc. 2018;1979(1):100014.

16. Gottfried JL, Pesce-Rodriguez RA, Farrow D, Dellinger J. Laboratory-scale investigation of the influence of ageing on the performance and sensitivity of an explosive containing ε-CL-20. Propellants Explos Pyrotech. 2018;43(6):616–625.

17. Gottfried JL, Smith DK, Wu C-C, Pantoya ML. Improving the explosive performance of aluminum nanoparticles with aluminum iodate hexahydrate (AIH). Sci Rep. 2018;8:8036.

18. Jiang Y, Deng S, Hong S, Zhao J, Huang S, Wu C-C, Gottfried JL, Nomura K-i, Li Y, Tiwari SC, Kalia RK, Vashishta P, Nakano A, Zheng X. Energetic performance of optically activated aluminum/graphene oxide composites. ACS Nano. 2018;12:11366–11375.

19. Gottfried JL, Pesce-Rodriguez RA, Wu C-C. Validation of LASEM energy release predictions via detonation testing and analytical characterization. Aberdeen Proving Ground (MD): Army Research Laboratory (US); 2018 Oct. Report No.: ARL-TR-8557.

20. Miller KK, Gottfried JL, Walck SD, Pantoya ML, Wu C-C. Plasma surface treatment of aluminum nanoparticles for energetic material applications. Combust Flame. 2019;206:211–213.

21. Wainwright ER, Dean SW, Lakshman SV, Weihs TP, Gottfried JL. Evaluating compositional effects on the laser-induced combustion and shock velocities of Al/Zr-based composite fuels. Combust Flame 2019;213:357–368.

22. Gottfried JL, Dean SW, Wu C-C, De Lucia JFC. Optimizing the performance of aluminized explosives: laser-based measurements of energy release and spectroscopic diagnostics. Aberdeen Proving Ground (MD): CCDC Army Research Laboratory (US); 2020 Apr. Report No.: ARL-TR-8934.

23. Gottfried JL, Barnes BC. Higher time-resolution LASEM, part II: influence of plasma chemistry on the laser-induced shock waves of explosives. Aberdeen Proving Ground (MD): CCDC Army Research Laboratory (US); 2020 Aug. Report No.: ARL-TR-9026.

24. Tsuyuki K, Miura S, Idris N, Kurniawan KH, Lie TJ, Kagawa K. Measurement of concrete strength using the emission intensity ratio between Ca(II) 396.8 nm and Ca(I) 422.6 nm in a Nd:YAG laser-induced plasma. Appl Spectrosc. 2006;60(1):61–64.

25. Abdel-Salam ZA, Galmed AH, Tognoni E, Harith MA. Estimation of calcified tissues hardness via calcium and magnesium ionic to atomic line intensity ratio in laser induced breakdown spectra. Spectrochim Acta, Part B. 2007;62B(12):1343–1347.

26. Cowpe JS, Moorehead RD, Moser D, Astin JS, Karthikeyan S, Kilcoyne SH, Crofts G, Pilkington RD. Hardness determination of bio-ceramics using laser-induced breakdown spectroscopy. Spectrochim Acta, Part B. 2011;66(3–4):290–294.

27. Zapata F, Ferreiro-González M, García-Ruiz C. Interpreting the near infrared region of explosives. Spectrochim Acta, Part A. 2018;204:81–87.

28. Koch JD, Piecuch S, Lightstone JM, Carney JR, Hooper J. Time-resolved measurements of near infrared emission spectra from explosions: pure pentaerythritol tetranitrate and its mixtures containing silver and aluminum particles. J Appl Phys. 2010;108(3):036101.

29. Gottfried JL. Higher time-resolution LASEM, part III: influence of laser-induced plasma chemistry on the laser-induced shock waves of aluminized explosives. Aberdeen Proving Ground (MD): CCDC Army Research Laboratory (US); 2020 Aug. Report No.: ARL-TR-9025.

List of Symbols, Abbreviations, and Acronyms

Al	aluminum
Al_2O_3	alumina; aluminum oxide
AlO	aluminum monoxide
ARL	Army Research Laboratory
C	carbon
Ca	calcium
CCDC	US Army Combat Capabilities Development Command
CN	cyano radical
Cr	chromium
Cu	copper
Fe	iron
fps	frames per second
H	hydrogen
ICCD	intensified charge-coupled device
IR	infrared
LASEM	laser-induced air shock from energetic materials
Li	lithium
Mg	magnesium
micron-Al	micrometer-sized Al particles
Mn	manganese
Na	sodium
nano-Al	Al nanoparticles
NIR	near-infrared
ns	nanoseconds
O	oxygen
PMT	photomultiplier tube
RSD	relative standard deviation
Si	silicon

Ti	titanium
TNT	trinitrotoluene
UV	ultraviolet
VIS	visible
Zn	zinc

1 DEFENSE TECHNICAL
(PDF) INFORMATION CTR
DTIC OCA

1 CCDC ARL
(PDF) FCDD RLD CL
TECH LIB

1 CCDC ARL
(PDF) FCDD RLW LB
J GOTTFRIED